

## THE IMPACT OF GAS BULK ROTATION ON THE LYMAN- $\alpha$ LINE

JUAN N. GARAVITO-CAMARGO<sup>1</sup>, JAIME E. FORERO-ROMERO<sup>1</sup>, MARK DIJKSTRA<sup>2</sup>

*Submitted for publication in ApJ*

### ABSTRACT

We present results of radiative transfer calculations to measure the impact of gas bulk rotation on the morphology of the Lyman  $\alpha$  emission line in distant galaxies. We model a galaxy as a sphere with a homogeneous mixture of dust and hydrogen at a constant temperature. These spheres have a solid-body rotation with maximum velocities in the range  $0 - 300 \text{ km s}^{-1}$  and neutral hydrogen optical depths in the range  $\tau_H = 10^5 - 10^7$ . We also consider two kinds of spatial distribution for the radiation sources with respect to the sphere: central and homogeneous. Our main finding is that the line width and the intensity at the line's center increase with rotational velocity. For homogeneously distributed sources the line becomes single peaked at rotational velocities larger than the line width in the static case. Under the same conditions the escape fraction increases  $\sim 30\%$ . For radiation sources located off-center, the line morphology presents a range of single, double and triple peaks. We show how these results are useful to interpret recent spectroscopic results of distant  $z \sim 2 - 3$  star forming galaxies.

*Subject headings:* galaxies: high-redshift, galaxies: star formation, line: formation

### 1. INTRODUCTION

The detection of strong Ly $\alpha$  emission lines has become an essential method in extra-galactic astronomy to find distant star-forming galaxies (Partridge & Peebles 1967; Rhoads et al. 2000; Gawiser et al. 2007; Koehler et al. 2007; Ouchi et al. 2008; Yamada et al. 2012; Schenker et al. 2012). The galaxies detected using this method receive the name of Ly $\alpha$  emitters (LAEs). A detailed examination of this galaxy population has diverse implications for galaxy formation, reionization and the large scale structure of the Universe. Attempts to fully exploit the physical information included in the Ly $\alpha$  line require an understanding of all the physical factors involved in shaping the line. Due to the resonant nature of this line, these physical factors notably include temperature, density and bulk velocity field of the neutral Hydrogen in the emitting galaxy and its surroundings.

A basic understanding of the quantitative behavior of the Ly $\alpha$  line has been reached through analytic studies in the case of a static configurations, such as uniform slabs (Harrington 1973; Neufeld 1990) and uniform spheres (Dijkstra et al. 2006). Analytic studies of configurations including some kind of bulk flow only include the case of a sphere with a Hubble like expansion flow (Loeb & Rybicki 1999).

A quantitative description of the Ly $\alpha$  line has been reached through Monte Carlo simulations (Auer 1968; Avery & House 1968; Adams 1972). In the last two decades these studies have become popular due to the availability of computing power. Early into the 21st century, the first studies focused on homogeneous and static media (Ahn et al. 2000, 2001; Zheng & Miralda-Escudé 2002); Later on, the effects of clumpy media (Hansen & Oh 2006) and expanding/contracting shell/spherical geometries started to be studied (Verhamme et al. 2006;

Dijkstra et al. 2006). Similar codes have applied these results to semi-analytic models of galaxy formation (Orsi et al. 2012) and results of large hydrodynamic simulations (Forero-Romero et al. 2011, 2012; Behrens & Niemeyer 2013). Recently, Monte Carlo codes have also been applied to the results of high resolution hydrodynamic simulations of individual galaxies (Laursen et al. 2009; Barnes et al. 2011; Verhamme et al. 2012; Yajima et al. 2012). Meanwhile, recent developments have been focused on the systematic study of clumpy outflows (Dijkstra & Kramer 2012) and anisotropic velocity configurations (Zheng & Wallace 2013).

The recent studies of galaxies in hydrodynamic simulations (Laursen et al. 2009; Barnes et al. 2011; Verhamme et al. 2012; Yajima et al. 2012) have all shown systematic variations in the Ly $\alpha$  line with the viewing angle. These variations are a complex superposition of anisotropic density configurations (i.e. edge-on vs. face-on view of a galaxy), the inflows observed by gas cooling and the outflows included in the supernova feedback process of the simulation. These bulk flows physically correspond to the circumgalactic and intergalactic medium (CGM and IGM). These effects are starting to be studied in simplified configurations that vary the density and wind characteristics (Zheng & Wallace 2013).

However, in all these efforts the effect of rotation, which is an ubiquitous feature in galaxies, has not been systematically studied. The processing of the Ly $\alpha$  photons in a rotating interstellar medium (ISM) must have some kind of impact in the Ly $\alpha$  line morphology.

Performing that study is the main goal of this paper. We investigate for the first time the impact of rotation on the morphology of the Ly $\alpha$  line. We focus on a simplified system: a spherical gas cloud with homogeneous density and solid body rotation, to study the line morphology and the escape fraction in the presence of dust. We base our work on two independent Monte Carlo based radiative transfer codes CLARA (Forero-Romero et al. 2011) and XX (Dijkstra & Kramer 2012).

<sup>1</sup> Departamento de Física, Universidad de los Andes, Cra. 1 No. 18A-10, Edificio Ip, Bogotá, Colombia

<sup>2</sup> Max Planck Institute for Astrophysics, Karl-Schwarzschild-Str. 1, 85741, Garching, Germany

This paper is structured as follows: In §2 we present the implementation of bulk rotation into the Monte Carlo codes, paying special attention to coordinate definitions. We also list the different physical parameters in the simulated grid of models. In the next §3 we present the results of the simulations, with special detail to quantities in the line that show a clear evolution as a function of the sphere rotational velocity. In §4 we discuss the implications of our results in the interpretation of LAEs observations and further refinements that can be implemented in the theoretical modeling of the Ly $\alpha$  line. In the last section we present our conclusions.

In this paper we express a photon's frequency in terms of the dimensionless variable  $x \equiv (\nu - \nu_a)/\Delta\nu_\alpha$ , where  $\nu_\alpha = 2.46 \times 10^{15}$  Hz is the Ly $\alpha$  resonance frequency,  $\Delta\nu_\alpha \equiv \nu_\alpha \sqrt{2kT/m_p c^2} \equiv \nu_a v_{th}/c$  is the Doppler broadening of the line which depends on the neutral gas temperature  $T$  scattering the radiation or equivalently the thermal velocity  $v_{th}$  of the atoms.

## 2. MODELS OF BULK GAS ROTATION

Describing the kinematics of gas rotation in all generality is a complex task, specially at high redshift where there is still missing a thorough observational account of rotation in galaxies beyond  $z > 1.0$ . Even at low red-shifts there is a great variation in the shape of the rotation curve as observed in HI emission as a function of the distance to the galaxy center. However there are two recurrent features. First, in the central galactic region the velocity increases proportional to the radius, following a solid rotation behavior. Second, beyond a certain radius the rotation curve tends to flatten.

An ab-initio description of realistic rotation curves in simulations depends on having access to the dynamic evolution of all mass components in the galaxy: stars, gas and dark matter. Such level of realism is extremely complex to achieve, specially if one wants to get a systematic description based on statistics of simulated objects.

Following the tradition of studies of Ly $\alpha$  emitting systems, we implement a model with simplified geometry. We assume that the gas is homogeneously distributed in a sphere that rotates as a solid body with constant angular velocity. This simple model will contain only one free parameter: the linear velocity at the sphere's surface,  $V_{max}$ .

### 2.1. Detailed Implementation of Rotation

In the Monte Carlo code we define a Cartesian coordinate system to describe the position of each photon. The origin of this system coincides with the center of the sphere and the rotation axis is defined to be  $z$ -axis. With this choice, the components of the gas bulk velocity field,  $\vec{v} = v_x \hat{i} + v_y \hat{j} + v_z \hat{k}$ , can be written as

$$v_x = -\frac{y}{R} V_{max}, \quad (1)$$

$$v_y = \frac{x}{R} V_{max}, \quad (2)$$

$$v_z = 0, \quad (3)$$

where  $R$  is the radius of the sphere and  $V_{max}$  is the linear velocity at the sphere's surface. The minus/plus sign in the  $x/y$ -component of the velocity indicates the direction

Physical Parameter (units)	Symbol	Values
Velocity (km s <sup>-1</sup> )	$V_{max}$	0, 50, 100, 200, 300
Hydrogen Optical Depth	$\tau_H$	10 <sup>5</sup> , 10 <sup>6</sup> , 10 <sup>7</sup>
Dust Optical Depth	$\tau_a$	0, 1
Photons Distributions		Central, Homogeneous

TABLE 1

LIST OF THE PHYSICAL PARAMETERS THAT DEFINE THE SPHERICAL MODELS SIMULATED IN OUR MONTE CARLO CALCULATIONS. FOR EACH PARAMETER WE VARY THE VALUES IN THE RANGE LISTED IN THE LAST COLUMN. TAKING INTO ACCOUNT ALL THE POSSIBLE COMBINATIONS WE END UP WITH 60 DIFFERENT MODELS.

of rotation. In this case we take the angular velocity in the same direction as the  $\hat{k}$  unit vector. With these definitions we can write the angular velocity as  $\omega = V_{max}/R$ .

For each photon in the simulation we have its initial position inside the sphere, direction of propagation  $\hat{k}_{in}$  and reduced frequency  $x_{in}$ . The photon's propagation stops once they cross the surface of the sphere. At this point we store the position, the outgoing direction of propagation  $\hat{k}_{out}$  and the reduced frequency  $x_{out}$ . We define the angle  $\Theta$  by  $\cos \Theta = \hat{k} \cdot \hat{k}_{out}$ , that is the polar angle of the outgoing photon with respect to the  $z$  axis. Following Zheng & Wallace (2013) we make the study of the anisotropic emission in terms of this angle..

### 2.2. Grid of Simulated Galaxies

In the Monte Carlo calculations we follow the propagation of  $N_\gamma = 10^5$  numerical photons through different spherical galaxies. For each galaxy we vary at least one of the following parameters: the maximum rotational velocity  $V_{max}$ , the hydrogen optical depth  $\tau_H$ , the dust optical depth  $\tau_a$  and the initial distribution of photons with respect to the gas. There are 60 models initial combining all variations of the input parameters. Table 1 summarizes the models.

Additionally, we have used two independently developed Monte Carlo codes Forero-Romero et al. (2011); Dijkstra & Kramer (2012) to perform the calculations of the non-dusty models. The results we report are robust in the sense that they are obtained by both codes.

### 2.3. Brief Description of the Radiative Transfer Codes

Here we briefly describe the relevant points for the two radiative transfer codes we have used. For a detailed description we refer the reader to the original papers Forero-Romero et al. (2011); Dijkstra & Kramer (2012).

The codes follow the individual scatterings of Ly $\alpha$  photons as it travels through a 3D distribution of neutral Hydrogen. At each scattering the frequency of the photon (in the laboratory frame) and its direction of propagation change. This change in frequency is due to the peculiar velocities of the Hydrogen atom that absorbed and reemitted the photon. If dust is present, the photon can interact either with a Hydrogen atom or dust grain. In the case of a dust interaction the photon can be either absorbed or scattered, this probability is encoded in the dust albedo,  $A$ , which we chose to be 1/2. In order to obtain accurate values for the escape fraction of photons in the presence of dust, we do not use any accelerating mechanism in the radiative transfer. Once the photons escape the gas distribution we store their direction at

their direction of propagation and frequency at their last scattering.

The photons are thus emitted in some region of the gas distribution and follow a random walk in space and frequency until they escape the gas distribution or are absorbed by a dust grain. The initialization process for the Ly $\alpha$  photons has to specify its position, frequency and direction of propagation. In our case we select the initial frequency to be exactly the Ly $\alpha$  restframe frequency ( $x = 0$ ) and the direction of propagation to be random following an flat probability distribution over the sphere.

The gas is completely defined by its geometry (i.e. sphere or slab), temperature  $T$ , Hydrogen optical depth  $\tau_H$ , dust optical depth  $\tau_a$  and the bulk velocity field  $\vec{v}$ . Here we treat the gas as homogeneous in density ( $\tau_H$ ,  $\tau_a$ ) and temperature.

### 3. RESULTS

The central result of this paper is summarized in Figure 1. It shows the evident impact of rotation on the morphology of the emergent Ly $\alpha$  line. Both panels focus on the results for  $\tau_H = 10^7$ , showing that the influence of rotation is present both when the photons are either homogeneously or centrally initialized over the gas volume.

In the next subsections we characterize the line morphology by the half-width at half intensity and the peak maxima. In order to interpret the morphological changes in the line we also report the median number of scatter for each Ly $\alpha$  photon in the simulation. For the models where dust is included we measure the escape fraction as a function of rotational velocity. Finally, we make an estimate of the anisotropic emission of the models in comparison with static spheres.

#### 3.1. Line width and peak maxima

The first quantitative conclusion of the effect of rotation in the Ly $\alpha$  line is that double peaks broaden and reduce their intensity while the line center rises. This gives the impression that, as the rotational velocity increases, the double peaks are merged into a single broad emission peak. This is most evident at the highest rotational velocities for the homogeneously distributed sources (right panel in Figure 1).

To quantify the line broadening we use the width at half maximum (FWHM),  $W_{1/2}$ . Figure 2 shows how  $W_{1/2}$  increases with rotational velocity. Continuous (dashed) lines connect the results for homogeneous (central) source distribution. For the temperature  $T = 10^4$ K used in our radiative transfer calculations the thermal velocity is  $v_{th} = 12.8$  km s $^{-1}$ . For a model with  $\tau_H$  it means that the FWHM increase up to 350 km s $^{-1}$  (at  $V_{max} = 300$  km s $^{-1}$ ) compared to 150 km s $^{-1}$  in the static case.

Figure 3 shows the position for the peak maxima as a function of the rotational velocity  $V_{max}$ . This Figure clearly shows that in the case of central distributed sources there is barely any change with rotational velocity in the range of explored parameters. However, in the case of homogeneously emitted sources the maxima position remain close to constant until beyond some velocity threshold the line becomes single peaked with  $x_m = 0$  km s $^{-1}$ .

The transition to a single peaked line seems to occur in systems where it is easier for the bulk of the photons to escape with the lowest number of scatterings possible, allowing them not to move very far from the center of the line. This might explain how the single peak stage is easily achieved in the homogeneous source distribution. In this case there is a fraction of the photons that are inside a photo-sphere region with  $\tau_{H,r} \ll \tau_H$  where  $\tau_{H,r}$  is the optical depth from the radius of emission to the sphere's surface. These conditions allows the photons to escape with much less scatterings compared to the photons emitted at the very center of the sphere. In turn, it gives the photons less scatterings to be placed far from the line center.

Increasing the rotational velocity  $V_{max}$  reduces the optical depth making the photo-sphere region effectively larger, increasing the number of photons escaping close to the line's center. In our models we find the following correspondence between the optical depth  $\tau_H = \{10^5, 10^6, 10^7\}$  and the transitional velocities  $V_{trans} = \{50 - 100 \text{ km s}^{-1}, 100 - 200 \text{ km s}^{-1}, 200 - 300 \text{ km s}^{-1}\}$  which can only be constrained to be in the range of velocities in the models that gave a  $x_{max} \neq 0$  and  $x_{max} = 0$ .

For the central emission the transition to a single peak is never completed in the range of explored parameters. The non appearance of a single peak phase can be in part explained to the absence of a photo-sphere, as is the case in the homogeneous distribution. Nevertheless, there is a rise in the intensity at the line center as the rotational velocity increases. This hints that the encounters with a non static medium are inefficient in pushing photons outside the line's center.

In the next sub-section we quantify the number of scatterings and explore to what extent this is related to the emergence of single peaked emission.

#### 3.2. Average Number of Scatterings

The number of Ly $\alpha$  photon scatterings affects its final frequency after escaping the galaxy. In static gas geometries, a large value of the optical depth correlates with a high number of scatterings, increasing the probability of finding a Ly $\alpha$  photon far from the center of the line. In these cases the peak maxima shifts away from the line center as the amount of neutral hydrogen increases.

In Figure 4 we show the average number of scatterings  $\langle N_{scatt} \rangle$  as a function of the rotational velocity  $V_{max}$ . For the central distributions the average number of scatterings has a modest change for increasing rotational velocities,  $\langle N_{scatt} \rangle$  changes less than 0.5% for different velocities. In the same set-up the average number of scatterings is proportional to the optical depth, as expected in analogy from the analytic result for the central infinite-slab  $\langle N_{scatt} \rangle = 1.612\tau_H$  (Adams 1972; Harrington 1973). In the spheres with centrally distributed sources we find  $\langle N_{scatt} \rangle = (1.50, 1.00, 0.92)\tau_H$  for optical depths  $\tau_H = (10^5, 10^6, 10^7)$ .

Figure 4 shows that for the homogeneous distribution there is a clear decrease of  $\langle N_{scatt} \rangle$  as the  $V_{max}$  increases. This effect is more pronounced for lower values of the optical depth. For  $\tau_H = 10^5$  the average number of scatterings decreases by 61% at  $V_{max} = 300$  km s $^{-1}$  in comparison to the static case.

The analytic expectation for the average number of

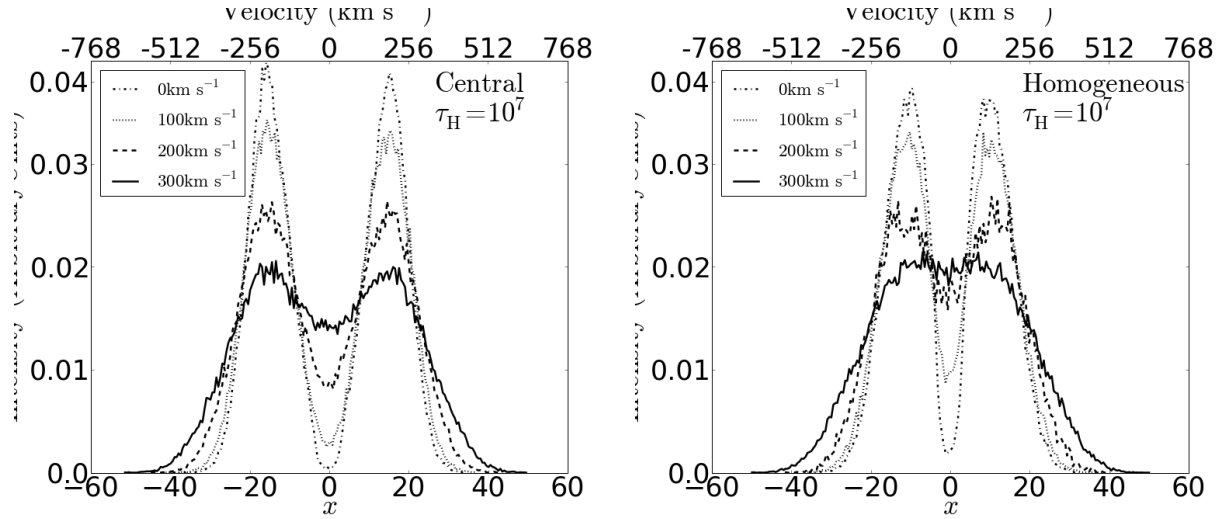


FIG. 1.— Shape of the Ly $\alpha$  line for different velocities rotational velocities for spherical distributions with  $\tau_H = 10^7$ . The left (right) panel shows the central (homogeneous) photon distribution. All photons were taken into account regardless of their final direction of propagation.

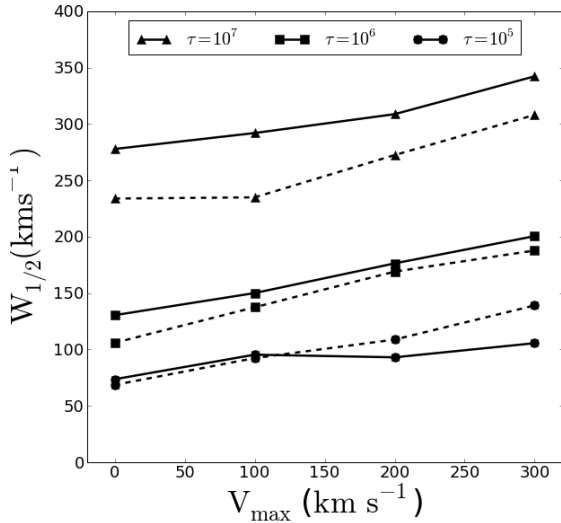


FIG. 2.— Half-width for the non-dusty models as a function of rotational velocity  $V_{\max}$ . Continuous (dashed) lines correspond to central (homogeneous) source distributions.

scatterings in a slab with homogeneously distributed sources is  $\langle N_{\text{scatt}} \rangle = 1.16\tau_H$  (Harrington 1973). This is 0.72 times lower than the same case with photons emitted in the slab's center. In our case we find that for the static case and the homogeneously distributed sources  $\langle N_{\text{scatt}} \rangle = (0.99, 0.59, 0.51)\tau_H$ , this represents factors of (0.66, 0.59, 0.55) lower than the centrally emitted photons.

In order to gain a deeper understanding of these results we make 2D histograms for the number of scatterings as a function of the outgoing dimensionless frequency  $x$ . In Figure 5 we show such histogram in the case  $\tau_H = 10^5$  for the static case and  $V_{\max} = 300 \text{ km s}^{-1}$ . The upper (lower) panels show the results for the homogeneous (central) source distribution. The color scale is logarithmic in the number of photons at a certain value  $x - N_{\text{scatt}}$ .

The top right panel of Figure 5 supports our hypothesis

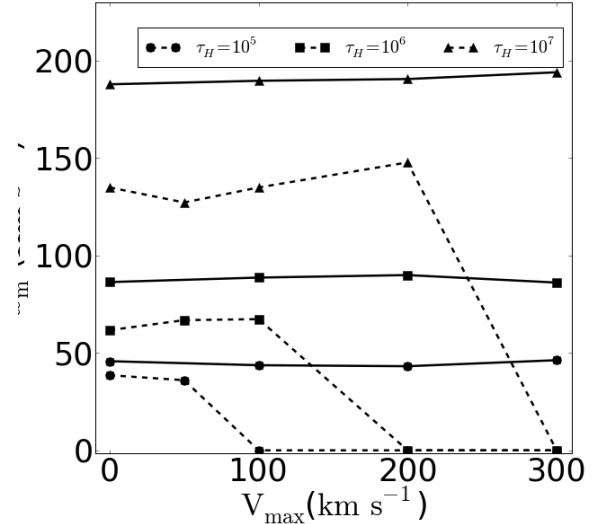


FIG. 3.— Position of the peak maxima as a function of rotational velocity  $V_{\max}$ . Continuous (dashed) lines correspond to central (homogeneous) source distributions. A value of  $x_{\max} = 0$  indicates that line becomes single peaked.

about the photo-sphere in the homogeneous distribution. In that case most of the photons that left with  $x \sim 0$  have escaped with less than 10 scatterings. This explains the origin of a single central peak. However, for a central distribution the situation is different (lower panels). In this case the number of scatterings remains high, in the order of the optical depth, but the two peaks do get closer to each other. In this case the physical picture is that each scattering, due to the bulk velocity of the gas, is inefficient in driving the photon outside the line center.

### 3.3. Dusty Clouds: Escape Fraction

The average number of scatterings is also reflected in the amount of photons absorbed by dust. Under these considerations we do not expect any change in the escape fraction for a dusty cloud with central source of

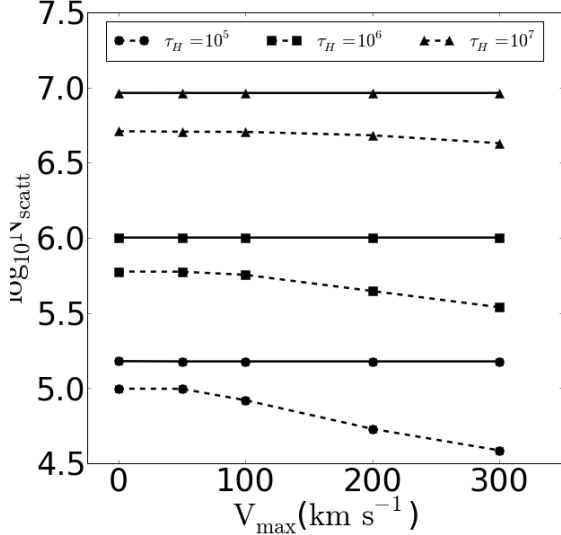


FIG. 4.— Logarithm of the average number of scatterings as function of rotational velocity. Continuous (dashed) lines represent a central (homogeneous) distribution of sources.

radiation given that the number of scatterings remains close to constant. On the other hand, in the case of a homogeneous radiation source the number of scatterings drops as  $V_{\max}$  increases, which has to be reflected as an increasing escape fraction.

Figure 6 shows the dependence of the escape fraction as a function of the maximum rotational velocity, confirming our expectations. For the central source distribution the escape fraction barely shows any change, while for the homogeneous case there is a clear increase in the escape fraction for high rotational velocities. Rotation has a higher relative impact in the models with low optical depth  $\tau_H = 10^5, 10^6$ , where it can rise from (0.26, 0.28) ( $V = 0 \text{ km s}^{-1}$ ) up to (0.37, 0.39) ( $V_{\text{rot}} = 300 \text{ km s}^{-1}$ ).

In Figure 7 we put these results in the context of the analytic solution for the infinite slab (Neufeld 1990). In Neufeld’s set-up the analytic solution depends uniquely on the product  $(a\tau_H)^{1/3}\tau_a$ , an approximation that is valid only in the limits where  $a\tau_H \gg 1$ . The dashed lines in Figure 7 correspond to the cases of different velocities. First of all we note that the escape fraction does not increase from  $\tau_H = 10^5$  to  $\tau_H = 10^6$ , this is explained since there is a transition from an opaque to an extremely opaque medium which affects how Ly $\alpha$  photons escape from the medium: single flight vs single excursion. This figure also shows that the escape fraction is higher by factors of 2 – 10 than the expectation for a slab with centrally distributed sources. Furthermore, the decrease of the escape fraction with increasing optical depth is also slower.

#### 3.4. Off-Centered emission

The raw data from the model with homogeneous radiation sources allows to study the effect of radiation sources distributed with a different symmetry than the gas. We can select photons emitted in off-centered spheres with respect to the gas distribution and check whether this produces asymmetries in the line.

Figure 8 shows the two spherical regions we define to

test for this effect. Each has a radius of  $0.5R$  and can have two possible centers positions  $C$  along the  $\hat{j}$  direction:  $\pm C\hat{i}$ . We also place an observer along the  $\hat{j}$  direction, such that the emitting sphere centered on  $+C\hat{j}$  moves away from the observer and the sphere centered on  $-C\hat{j}$  moves towards the observer.

We study first the angular deviations of the outgoing photons with respect to an isotropic flux. We follow Zheng & Wallace (2013) to estimate the flux as a function of the angle  $\Theta$  formed by the outgoing photons and the observer. This is expressed by

$$F(\mu) = \frac{2\Delta N}{N\Delta\mu}, \quad (4)$$

where  $\mu = \cos\Theta$ ,  $N$  is the total number of outgoing photons,  $\Delta N$  is the number of photons in a angular bin  $\Delta\Theta$ . This definition satisfies the condition  $\int_{-1}^1 F(\mu)d\mu/2 = 1$ .

The variations in the  $\mu$  distribution is shown in Figure 9, for the Off-Center model there is a strong dependence of the observed flux on the relative position of an observer with  $\Delta\mu \leq 25\%$ . In contrast, the central and homogeneous source distributions only show a weak anisotropy at the level of  $\Delta\mu \leq 3\%$ . The variations in  $\mu$  does not depend on the rotational velocity while increasing the optical depth  $\tau_H$  would also increase the variation of  $\Delta\mu$  up to a 15%.

Figure 10 show the spectra for the two off-centered spheres located at  $C = \pm 0.5R$ . In this case we only use photons that have outgoing directions aligned with the observer i.e  $|\mu| > 0.9$  &  $|\mu| < 1.0$ . We do not find any asymmetry in the line produced by the off-center emission, the difference between the profiles corresponding to the spheres located at  $C = -0.5R$  and that ones located at  $C = 0.5R$  is negligible. As in the homogeneous/ central model the line gets broader as the rotational velocity increase also the central part of the line becomes predominant. There is also a signature of possible three peaks profiles for some models ( $\tau = 10^6, V = 100, 200 \text{ km s}^{-1}$  and  $\tau = 10^7, V = 200, 300 \text{ km s}^{-1}$ ) which would be studied in detail in the next section.

#### 3.5. Three-Peak Profiles

As mentioned above Off-centered emission shows signs of three peak profiles, to analyse this in more detail we use the same method of the spheres explained in §3.4. We select spheres at  $C = (\pm 0.25R, \pm 0.5R, \pm 0.75R)$  with a radii of  $0.25R$  for all the models, for those who present signs of three peak profiles such as ( $V_{\max} = 50 \text{ km s}^{-1}$  &  $\tau_H = 10^5$ ), ( $V_{\max} = 100 \text{ km s}^{-1}$  &  $\tau_H = 10^6$ ), ( $V_{\max} = 200 \text{ km s}^{-1}$  &  $\tau_H = 10^7$ ) we made another run with  $\tau_\gamma = 10^6$  with the aim of get stronger profiles.

Figure 11 shows our findings, in order to get such profiles a relation between optical depth, rotational velocity and  $C$  must be accomplish. In particular we found that for the outer spheres  $C = \pm 0.75$  the three peak arises for all of our models with  $\tau_\gamma = 10^6$  this is due to the fact that the wings of the line move away from the central part as  $C$  increase. Another requirement is that a high optical depth must be balanced with a high velocity in order to make the wings and the central peak similar in height, for models in which the velocity is low spheres at  $C = \pm 0.25$  produce noise three peak profiles due to the

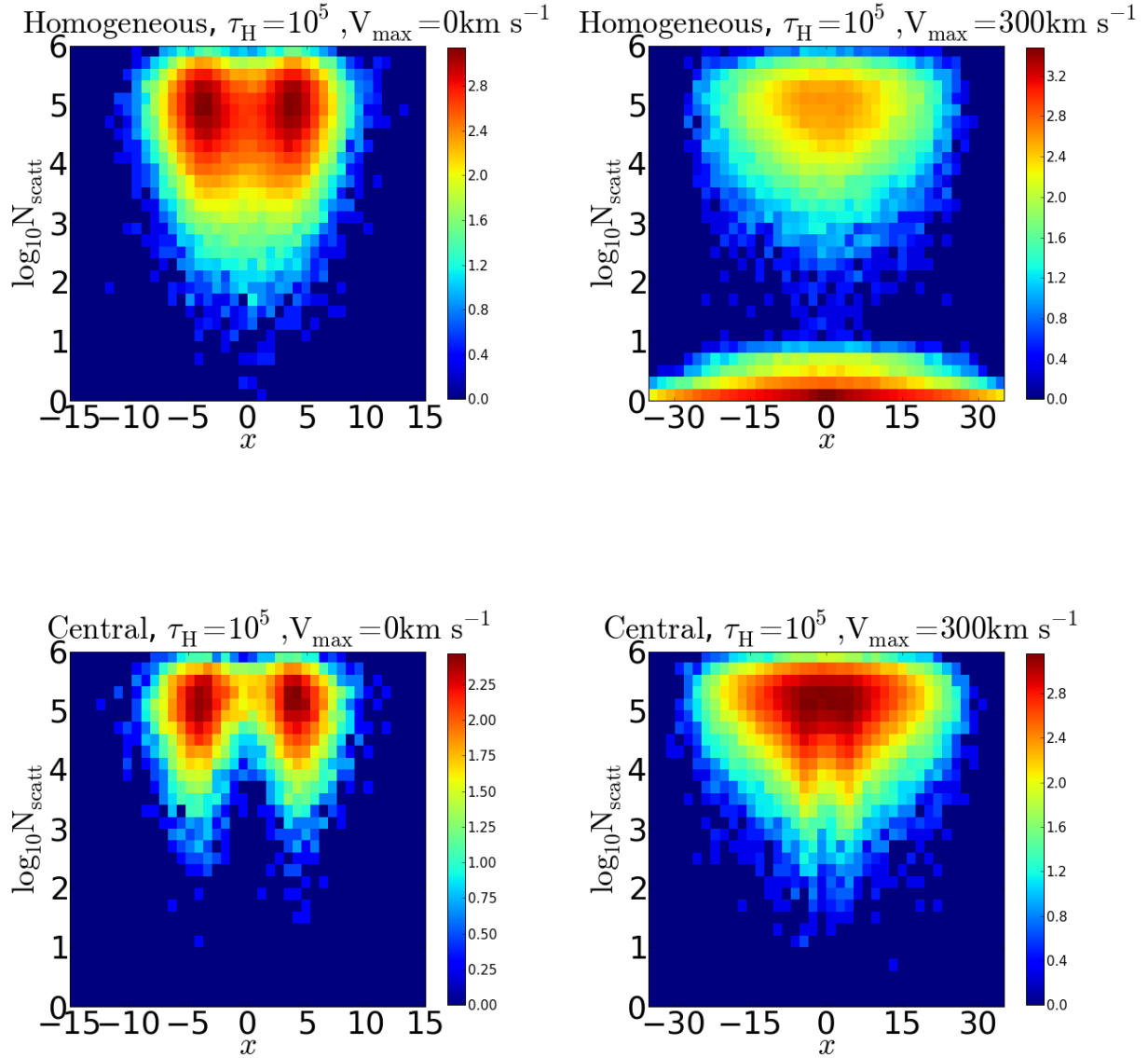


FIG. 5.— 2D histogram of  $N_{\text{scatt}}$  vs  $x$ . The upper (lower) panels show the homogeneous (central) source distribution. Left corresponds to the static case and the right  $V_{\text{max}} = 300 \text{ km/s}$ . The color scale is logarithmic on the number of photons with given values of  $N_{\text{scatt}}$  and  $x$ .

high value of  $\tau_{H,r}$ .

Figure 12 show that even with a low resolution a three-peak profile would be observed, this is important for observational porpoises due to the finite spectral resolution.

#### 4. DISCUSSION

Gas bulk rotation has a noticeable effect on the morphology of the  $\text{Ly}\alpha$  line. In this section we discuss the implications of these findings for the interpretation of available observational data. Our discussion focuses on the qualitative aspects of diverse morphological features observed by Kulas et al. (2012) and Yamada et al. (2012)

We follow a classification of  $\text{Ly}\alpha$  profiles made by Kulas et al. (2012). They presented observational results

for star forming galaxies at  $z = 2-3$  with multiple peaks in their  $\text{Ly}\alpha$  emission. They classified the observed lines into five groups. In Group I the red peak is stronger than the blue, while in Group II the blue peak is stronger, in both cases the peaks are symmetrically located around the line center. In Group III the blue peak also dominates but there is an overall redward shift of the zero point. Group IV presents two similar peaks symmetrically located around the zero point and Group V galaxies show three peaks.

The asymmetries in Groups I, II and III cannot be explained by rotation. However, some galaxies in those groups have a high flux between the two peaks; an effect

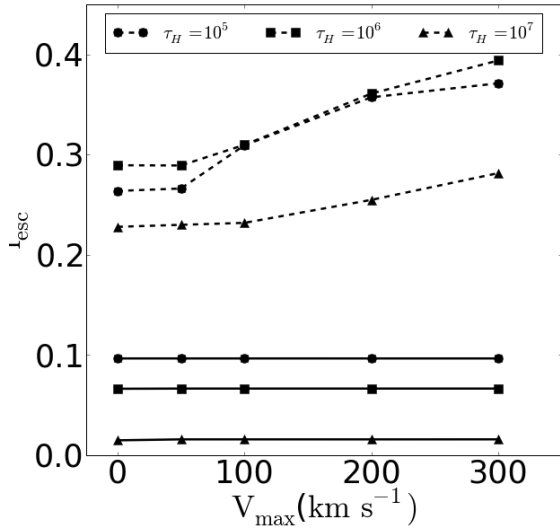


FIG. 6.— Escape fraction as a function of rotational velocity, for these models we took  $\tau_a = 1$ . The continuous (dashed) lines correspond to central (homogeneous) models.

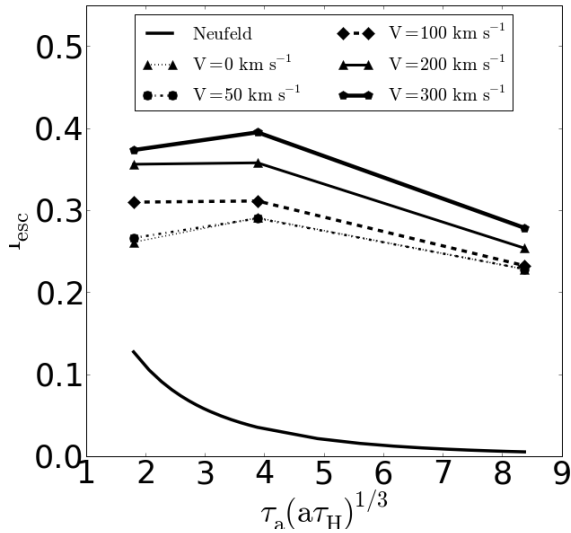


FIG. 7.— Escape fraction as a function of the product  $(a\tau_H)^{1/3}\tau_a$ . The analytic solution for the infinite slab is shown as a continuous line. Different dashed lines correspond to different rotational velocities, for this models  $\tau_a = 1$ .

that can be induced by rotation. The same argument applies to galaxies in the group IV in which the flux in between of the two peaks is high ( $\geq 70\%$  of the intensity in the highest peak). Finally, the triple peaked lines in Galaxies in Group V can be easily reproduced by rotation with off-centered emission given the right amount of asymmetry between the emitting region and neutral hydrogen distribution.

Another relevant sample of observations was presented by Yamada et al. (2012) for 91 LAEs at  $z = 3.1$ . They find that  $\sim 33\%$  of the galaxies present a single peak profile. Some of the peaks have a strong symmetry, while others do not. The symmetric single peaked profile can be explained by rotation effects, while the asymmet-

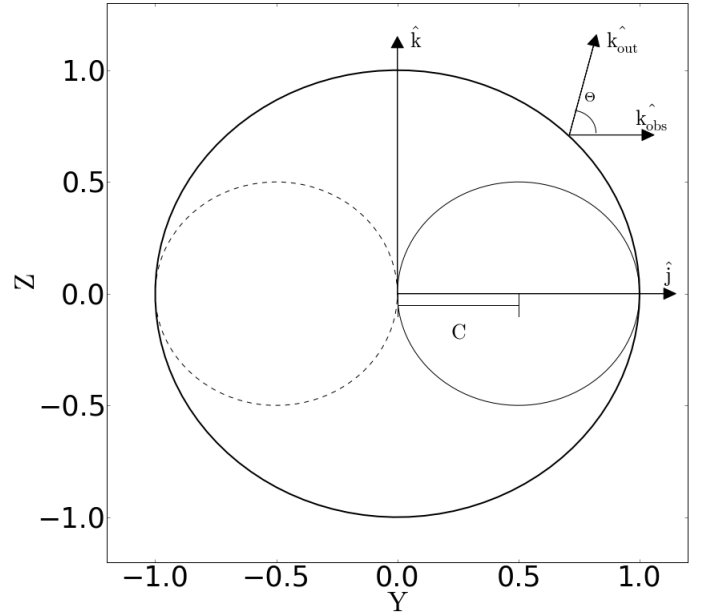


FIG. 8.— The two solid circles show the two different spherical off-centered emitting regions. The angular velocity vector is defined to be along the  $\hat{i}$  direction (where the reader is) and the observer is along the  $\hat{j}$  direction.

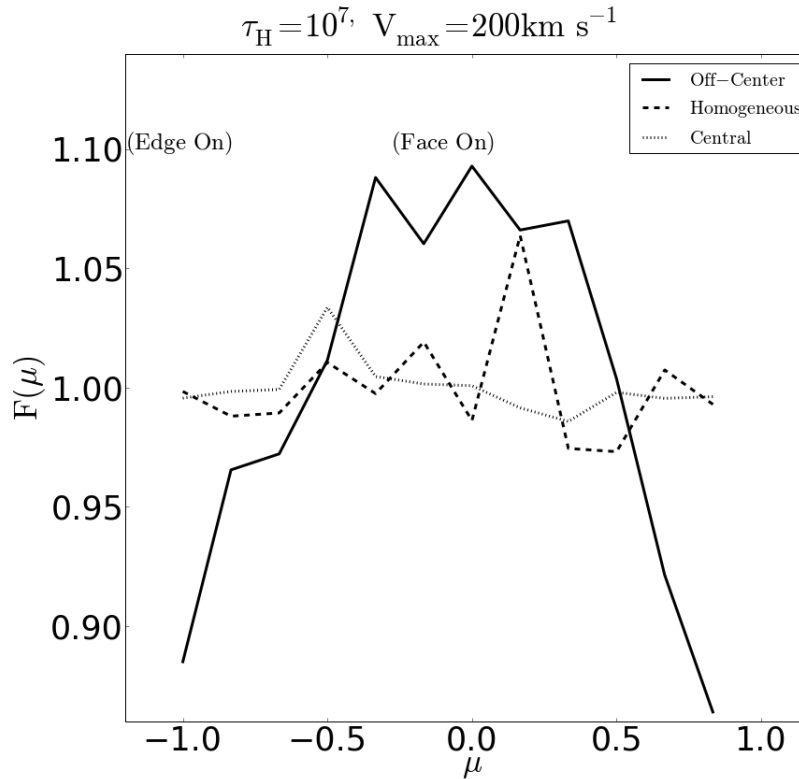


FIG. 9.—  $\mu$  histogram showing the orientation effects for the different distributions central (Points line), homogeneous (Dashed) and off-Center (Solid line).

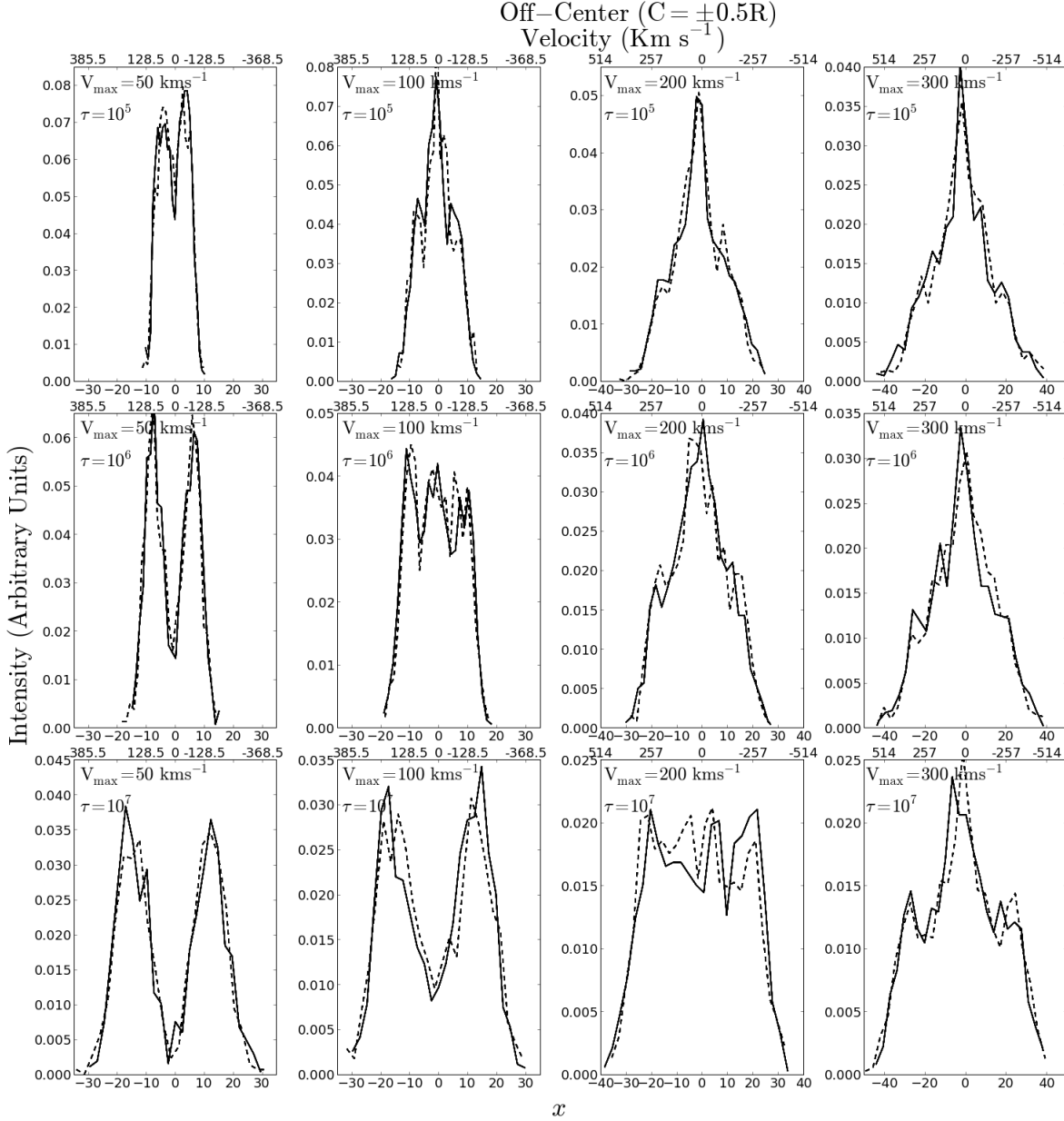


FIG. 10.—  $\text{Ly}\alpha$  profiles for the off-center positions for all of our models, Dashed/solid lines represents spheres centered at  $-0.5R/+0.5R$  respectively.

ric cases naturally arise in outflow/inflow models (Verhamme et al. 2008; Dijkstra et al. 2006). Among the 91 LAEs, 8 reveal triple peaked profiles with a central peak and two smaller peaks at the redder and bluer side, a feature that is present in our off-center emission models with rotation Figure 11.

The presence of single peaked profiles has been associated to inflow/outflow dynamics (?). In this paper we show that gas bulk rotation can also be considered as a probable origin for that behavior, provided that the observed single peak is highly symmetric. Similarly, in the case of double peaked lines with a high level of flux at the line center, rotation also deserves to be considered in the pool of possible bulk flows responsible for that feature, specially if the two peaks have similar intensities. The

case of triple peaked lines is another clear feature of gas rotation under the additional condition of an off-centered emission.

## 5. CONCLUSIONS

This paper quantifies for the first time in the literature the effects of rotation in the morphology of the  $\text{Ly}\alpha$  emission line in star forming galaxies. The results are based on the study of an homogeneous sphere of gas with solid body rotation. We explore a range of models by varying the rotational speed, hydrogen optical depth, dust optical depth and initial distribution of  $\text{Ly}\alpha$  photons with respect to the gas density. As a cross-validation, we obtain our results from two independently developed Monte-Carlo radiative transfer codes.

Our main result is that rotation clearly impacts the



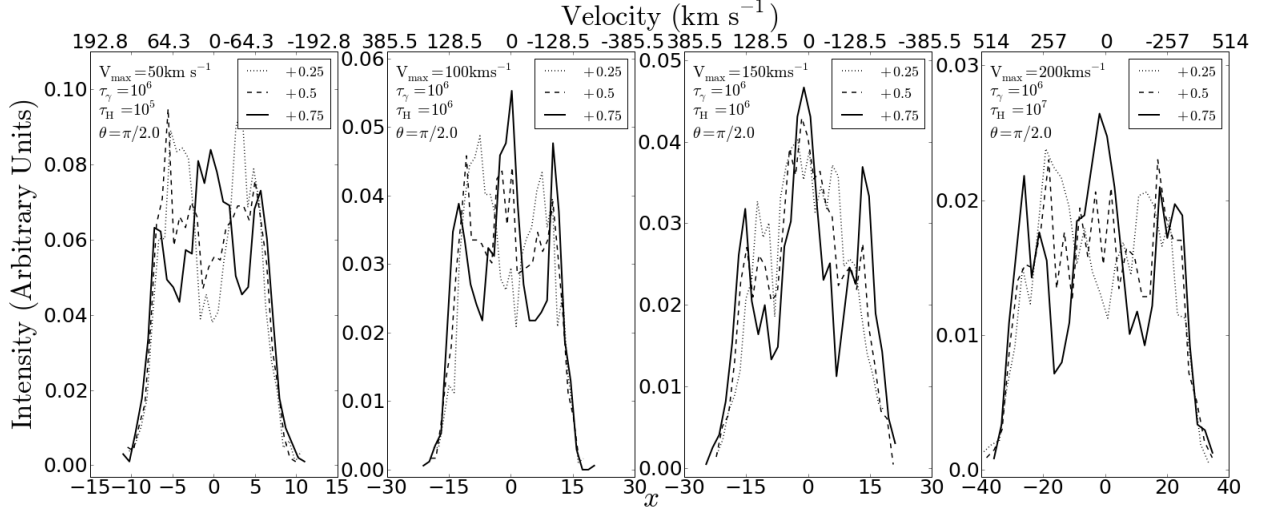


FIG. 11.— Three-Peak profiles for three different off-center positions  $C = 0.25R$  (dotted line),  $C = 0.5R$  (dashed line) &  $C = 0.75R$  (solid line) and for different rotational velocities.

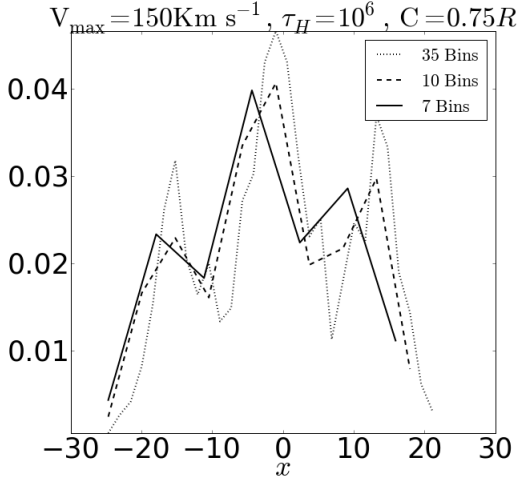


FIG. 12.— Three-Peak profiles for different resolutions: Low (Solid), medium (dashed), high (dotted),

$\text{Ly}\alpha$  line morphology. Double peaked lines can make transitions into single peaked lines as the rotational velocity increases. In the case of off-centered emission result into triple peaked lines for certain values of optical depth and rotational velocities.

Quantitatively the main results of our study are summarized in the following items.

- The line width increases with rotational velocity. The line width approximately follows the functional form  $W_{1/2}^2 = W_{1/2,0}^2 + (V_{\text{max}}/\lambda)^2$  where  $W_{1/2,0}$  indicates the line width for the static case.  $\lambda$  is a constant determined from the radiative transfer results it is  $\lambda_c = XX$  and  $\lambda_h = YY$  for the central and homogeneous source distribution, respectively.
- A single peaked line emerges for high rotational velocities in the case of homogeneously distributed sources. The cases of single peaked lines occur when the rotational velocity is larger than the line width measured in the static case.

- For central sources we find that the number of scatterings does not significantly decrease with rotation, this is due to the fact that the vast majority of scatterings events are resonant, during which the mean free path is very short and the effect of gas bulk rotation is not enough to affect  $\text{Ly}\alpha$  photons. The escape fraction does not depend on the rotational velocity neither the position of the peaks, but there is an increase in the flux on the central parts of the line for high rotational velocities.
- For homogeneous sources we find that the changes in the line morphology are linked to the reduction in the average number of scatterings. In the second part of §3.1 we show that, as rotational velocity increases, a large fraction of photons escape with less than 10 scatterings and on average with 40% less scatterings than in the static case. This makes highly improbable that a photon's frequency can move away from the line's center. In §3.1 For typical column densities of

$N_{HI} = 1e^{19} - 1e^{20}$ , we find that rotational velocities of 100-300 km s<sup>-1</sup> broaden the line profile up to a factor of 2–3 in comparison to the static case. Simultaneously, the flux in the line center also increases with rotational velocity. This increase induces the transition from a double peak to a single peak line in the models where the radiation sources are homogeneously distributed. Also the escape fraction increase by factors of 2–10 with respect to the slab with centrally sources.

- For non-symmetric sources we find that three peak profiles could emerge for models in which the rotational velocity is the necessary to give rise to a central peak, but not that high to decrease the amount of photons in the wings. When initial off-center sources are selected from the outer parts of the galaxy the wings of the line are stronger. Also we do not find any considerable asymmetries in the line produced by off-center emission.

Comparing our results with recent observed LAEs we find that many morphological features such as high central line flux, single peak profiles and multi-peaked profiles could be explained by gas bulk rotation present in these LAEs.

#### ACKNOWLEDGEMENTS

JNGC acknowledges financial support from Universidad de los Andes.

JEFR acknowledges financial support from Vicerrectoria de Investigaciones at Universidad de los Andes through a FAPA grant.

We thank the International Summer School on AstroComputing 2012 organized by the University of California High-Performance AstroComputing Center (UC-HiPACC) for providing computational resources where some of the calculations were done.

#### REFERENCES

- Adams, T. F. 1972, *ApJ*, 174, 439  
Ahn, S.-H., Lee, H.-W., & Lee, H. M. 2000, *Journal of Korean Astronomical Society*, 33, 29  
—. 2001, *ApJ*, 554, 604  
Auer, L. H. 1968, *ApJ*, 153, 783  
Avery, L. W., & House, L. L. 1968, *ApJ*, 152, 493  
Barnes, L. A., Haehnelt, M. G., Tescari, E., & Viel, M. 2011, *MNRAS*, 416, 1723  
Behrens, C., & Niemeyer, J. 2013, *A&A*, 556, A5  
Dijkstra, M., Haiman, Z., & Spaans, M. 2006, *ApJ*, 649, 14  
Dijkstra, M., & Kramer, R. 2012, *MNRAS*, 424, 1672  
Forero-Romero, J. E., Yepes, G., Gottlöber, S., Knollmann, S. R., Cuesta, A. J., & Prada, F. 2011, *MNRAS*, 415, 3666  
Forero-Romero, J. E., Yepes, G., Gottlöber, S., & Prada, F. 2012, *MNRAS*, 419, 952  
Gawiser, E., Francke, H., Lai, K., Schawinski, K., Gronwall, C., Ciardullo, R., Quadri, R., Orsi, A., Barrientos, L. F., Blanc, G. A., Fazio, G., & Feldmeier, J. J. 2007, *ApJ*, 671, 278  
Hansen, M., & Oh, S. P. 2006, *MNRAS*, 367, 979  
Harrington, J. P. 1973, *MNRAS*, 162, 43  
Koehler, R. S., Schuecker, P., & Gebhardt, K. 2007, *A&A*, 462, 7  
Kulas, K. R., Shapley, A. E., Kollmeier, J. A., Zheng, Z., Steidel, C. C., & Hainline, K. N. 2012, *ApJ*, 745, 33  
Laursen, P., Sommer-Larsen, J., & Andersen, A. C. 2009, *ApJ*, 704, 1640  
Loeb, A., & Rybicki, G. B. 1999, *ApJ*, 524, 527  
Neufeld, D. A. 1990, *ApJ*, 350, 216  
Orsi, A., Lacey, C. G., & Baugh, C. M. 2012, *MNRAS*, 425, 87  
Ouchi, M., Shimasaku, K., Akiyama, M., Simpson, C., Saito, T., Ueda, Y., Furusawa, H., Sekiguchi, K., Yamada, T., Kodama, T., Kashikawa, N., Okamura, S., Iye, M., Takata, T., Yoshida, M., & Yoshida, M. 2008, *ApJS*, 176, 301  
Partridge, R. B., & Peebles, P. J. E. 1967, *ApJ*, 147, 868  
Rhoads, J. E., Malhotra, S., Dey, A., Stern, D., Spinrad, H., & Jannuzi, B. T. 2000, *ApJ*, 545, L85  
Schenker, M. A., Stark, D. P., Ellis, R. S., Robertson, B. E., Dunlop, J. S., McLure, R. J., Kneib, J.-P., & Richard, J. 2012, *ApJ*, 744, 179  
Verhamme, A., Dubois, Y., Blaizot, J., Garel, T., Bacon, R., Devriendt, J., Guiderdoni, B., & Slyz, A. 2012, *A&A*, 546, A111  
Verhamme, A., Schaerer, D., Atek, H., & Tapken, C. 2008, 111, 89  
Verhamme, A., Schaerer, D., & Maselli, A. 2006, *A&A*, 460, 397  
Yajima, H., Li, Y., Zhu, Q., Abel, T., Gronwall, C., & Ciardullo, R. 2012, *ApJ*, 754, 118  
Yamada, T., Nakamura, Y., Matsuda, Y., Hayashino, T., Yamauchi, R., Morimoto, N., Kousai, K., & Umemura, M. 2012, *AJ*, 143, 79  
Zheng, Z., & Miralda-Escudé, J. 2002, *ApJ*, 578, 33  
Zheng, Z., & Wallace, J. 2013, *ArXiv e-prints*